**Shaowu Ning**
Applied Mechanics Laboratory,
School of Aerospace Engineering,
Tsinghua University,
Beijing 100084, China
e-mail: swning@qq.com

**Dongyang Chu**
Applied Mechanics Laboratory,
School of Aerospace Engineering,
Tsinghua University,
Beijing 100084, China
e-mail: 2277629255@qq.com

**Fengyuan Yang**
Applied Mechanics Laboratory,
School of Aerospace Engineering,
Tsinghua University,
Beijing 100084, China
e-mail: 1806856350@qq.com

**Heng Jiang**[1]
Key Laboratory of Microgravity,
Institute of Mechanics,
Chinese Academy of Sciences,
Beijing 100190, China;
University of Chinese Academy of Sciences,
Beijing 100049, China
e-mail: hengjiang@imech.ac.cn

**Zhanli Liu**[1]
Applied Mechanics Laboratory,
School of Aerospace Engineering,
Tsinghua University,
Beijing 100084, China
e-mail: liuzhanli@tsinghua.edu.cn

**Zhuo Zhuang**
Applied Mechanics Laboratory,
School of Aerospace Engineering,
Tsinghua University,
Beijing 100084, China
e-mail: zhuangz@mail.tsinghua.edu.cn

# Characteristics of Band Gap and Low-Frequency Wave Propagation of Mechanically Tunable Phononic Crystals With Scatterers in Periodic Porous Elastomeric Matrices

*The characteristics of passive responses and fixed band gaps of phononic crystals (PnCs) limit their possible applications. For overcoming this shortcoming, a class of tunable PnCs comprised multiple scatterers and soft periodic porous elastomeric matrices are designed to manipulate the band structures and directionality of wave propagation through the applied deformation. During deformation, some tunable factors such as the coupling effect of scatterer and hole in the matrix, geometric and material nonlinearities, and the rearrangement of scatterer are activated by deformation to tune the dynamic responses of PnCs. The roles of these tunable factors in the manipulation of dynamic responses of PnCs are investigated in detail. The numerical results indicate that the tunability of the dynamic characteristic of PnCs is the result of the comprehensive function of these tunable factors mentioned earlier. The strong coupling effect between the hole in the matrix and the scatterer contributes to the formation of band gaps. The geometric nonlinearity of matrix and rearrangement of scatterer induced by deformation can simultaneously tune the band gaps and the directionality of wave propagation. However, the matrix's material nonlinearity only adjusts the band gaps of PnCs and does not affect the directionality of wave propagation in them. The research extends our understanding of the formation mechanism of band gaps of PnCs and provides an excellent opportunity for the design of the optimized tunable PnCs and acoustic metamaterials (AMMs).* [DOI: 10.1115/1.4049516]

*Keywords: mechanically tunable phononic crystals, scatterer, periodic porous elastomeric matrix, band structure, directionality of wave propagation, geometric and material nonlinearities, wave propagation*

## 1 Introduction

Phononic crystals (PnCs) and acoustic metamaterials (AMMs) are periodic composite elastic media that have attracted a great deal of interest because they may exhibit unusual acoustic properties that are unavailable in natural materials [1,2]. Their well-defined architecture can filter, control, or guide the wave propagation in them [3–10]. Significantly, some PnCs and AMMs exhibit the characteristics of the band gap, in which the wave propagation is prohibited, and thus they can be used for vibration and noise control [11–16]. However, most PnCs and AMMs proposed to date are characterized by a passive response and operate at a fixed frequency range, limiting the number of possible applications. In recent years, various tunable PnCs and AMMs have been designed and realized using external stimuli, such as the temperature [17–20], electromagnetic field [21–26], electromechanical coupling [27], periodic shunted piezoelectric circuits [12,14–16,28], and mechanical control strategies [29–38].

In gas–solid or liquid–solid (the matrix material is gas or liquid and the scatterer is solid) PnCs, the scatterers of weak symmetry can be rotated to change unit cells' symmetry of PnCs so that their band structures can be manipulated [39–43]. For example, Goffaux and Vigneron [43] analyzed the manipulation performance of band gaps of PnC consisting of parallel solid square-section columns distributed in the air on a square lattice through the rotation of the columns. Due to the geometric anisotropy of the elliptical rids, Wu and Chen [41] investigated the dispersion characteristics of the two-dimensional sonic crystals consisting of elliptic rods in fluid and found that the refraction direction of the wave propagating through the sonic crystal is tuned by rotating the elliptic rods. However, this control strategy is not suitable for the manipulation of the band structures of solid–solid PnCs.

Periodic porous materials possess novel and unique properties, including lightweight, high energy absorption [44], and the ability to control the elastic wave's propagation, heat flow [45,46], and so on. The deformation mechanisms of the ligaments determine the properties and functionality of such materials. Especially, the periodic porous materials can be regarded as a special kind of

[1]Corresponding authors.

Contributed by the Applied Mechanics Division of ASME for publication in the Journal of Applied Mechanics. Manuscript received November 15, 2020; final manuscript received December 23, 2020; published online February 4, 2021. Assoc. Editor: Yonggang Huang.

  

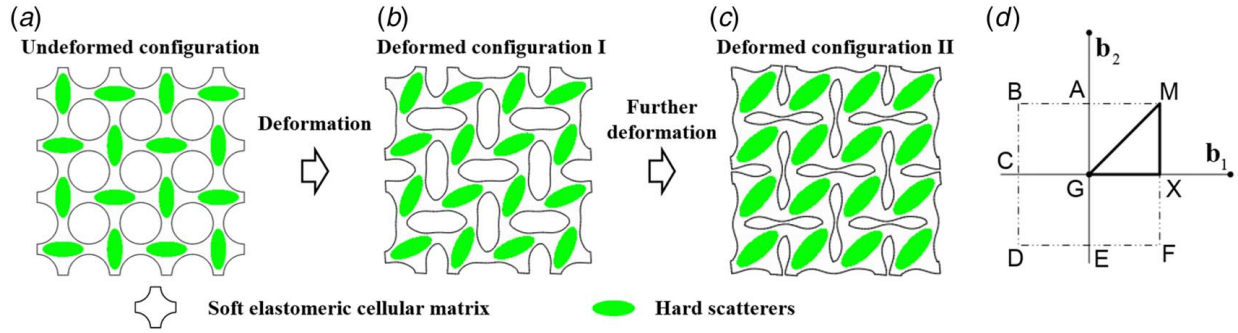


**Fig. 1 Schematic diagram of the designed tunable PnCs: (*a*) primitive configuration, (*b,c*) deformed configurations under equibiaxial compression, and (*d*) the first Brillouin zone (square, MBDF)**

PnCs, and they can be designed as a variety of structural forms. For example, Liu et al. [47] investigated the influence of the pore shapes (triangular, square, or circular) and the porosity on the band structures of PnCs with periodically distributed void pores. Especially, Bertoldi and coworkers [32,35,36] have initiated the exploration of soft porous periodic structures that can undergo reversible elastic deformations under the applied loads. Due to the post-buckling deformation, the geometrical configuration and tangent modulus of the soft periodic porous elastomeric structures can be significantly changed during deformation. The band gaps of these PnCs can be dramatically manipulated. Li et al. [37] proposed a design of soft composite materials consisting of stiff inclusions and voids periodically distributed in a soft matrix. The numerical and experimental results show that the post-buckling deformation could develop robustly by introducing the rigid inclusions into the periodic porous elastomeric matrix. Its band gaps could also be dramatically tuned during deformation. The introduction of stiff inclusion into periodic porous elastomeric matrix can increase the number and width of the phononic band gaps of the PnCs [38,48]. Meanwhile, it can also suppress the sensitivity of the post-buckling deformation to the geometrical imperfection so that their post-buckling deformation and band structures can be controlled in a robust way [37]. Differently, we pay attention to the sizeable rotational deformation of the periodic porous elastomeric matrix during deformation. Taking an example shown in Figs. 1(*a*)–1(*c*), we can notice that the rigid inclusion marked green rotates from an orthogonal state to a nonorthogonal state before and after deformation. Taking advantage of this phenomenon, we have designed a kind of PnCs consisting of multiple scatterers and soft periodic porous elastomeric matrices [48]. The analysis results show that introducing multiple scatterers into periodic porous elastomeric matrix can significantly enhance their band structures' tunability.

It is known that the arrangement of scatterers can alter the dynamic characteristics of the liquid/solid or gas/solid PnCs [39,40,43]. Meanwhile, the applied deformation can induce both geometric and material nonlinearities of the periodic porous elastomeric matrix. The band gaps and the directionality of wave propagation can be manipulated simultaneously [35]. For the PnC shown in Fig. 1, due to introducing the multiple scatterers into the periodic porous elastomeric matrix, the applied deformation can result in scatterers' rearrangements. It can change the coupling effect between the scatterers and the deformed holes. Like the liquid/solid or gas/solid PnCs, this design scheme can achieve the rotation of scatterer in the PnCs during deformation so that their band gaps can be significantly manipulated. However, it is not clear how these tunable factors control the tunable dynamic responses (band structure and directionality of wave propagation) of the PnCs during deformation. In this paper, we will focus on the influences of the coupling effect of scatterers and holes, geometric and material nonlinearities, and the arrangement of scatterers on the band structures of PnCs and directionality of wave propagation during deformation to reveal the roles of these tunable factors in the manipulation of dynamic characteristic of PnCs. The paper is organized as follows. The governing equations and material model, boundary conditions are presented in Sec. 2. In Sec. 3, we will investigate the roles of the above tunable factors in manipulating of band structures of PnCs and the directionality of wave propagation. Finally, conclusions are drawn in Sec. 4.

## 2 Calculation Model and Band Structures of Mechanically Tunable Phononic Crystals

**2.1 Descriptions of Calculation Model, Material Models, and Boundary Conditions.** The unit cell comprises a soft periodic porous elastomeric matrix with a void volume fraction of 50.27% and multiple scatterers (cylinder or elliptical cylinders) with a filling rate of 18.85%, as shown in Figs. 2(*c*)–2(*f*). The elastomeric material response is captured using a Neo-Hookean model. The strain energy density function of a Neo-Hookean material modified to include compressibility (with a high bulk modulus) is given by

$$W = C_{10}(\bar{I}_1 - 3) + \frac{1}{D_1}(J-1)^2 \tag{1}$$

where $C_{10} = \mu/2$, $D_1 = 2/\kappa$, $\mu = E/[2(1+\nu)]$, and $\kappa = E/[3(1-2\nu)]$. $\mu$, $\kappa$, $E$, and $\nu$ denote the initial shear, bulk modulus, Young's modulus, and Poisson's ratio, respectively. Here, we consider an elastomeric material with $\mu = 1.08 \times 10^6$ Pa, $\kappa = 2.0 \times 10^9$ Pa, and $\rho_0 = 1050\ \mathrm{kg/m^3}$ for the matrix material [35]. In contrast, it is assumed that the material of scatterer is elastic and they are fabricated using aluminum with shear modulus $\mu_{\mathrm{Al}} = 2.87 \times 10^{10}$ Pa, Poisson's ration $\nu_{\mathrm{Al}} = 0.352$ and density $\rho_{\mathrm{Al}} = 2730\ \mathrm{kg/m^3}$. In this paper, the commercial finite element code ABAQUS/Standard is used for numerical analysis. Assuming plane strain conditions, ABAQUS element type CPE6H is used to construct the finite element models of PnCs.

Here, we hope to control the wave propagation through the deformation of the matrix. It is well known that, under equibiaxial compression, the geometric pattern of the soft periodic porous elastomeric matrix can suddenly change due to mechanical instability (microscopic instabilities or macroscopic instabilities) [49,50]. In the processes of buckling analysis and post-buckling analysis, continuous periodic boundary conditions are imposed on all cell boundaries such that

$$\mathbf{u}_{\mathrm{B}} - \mathbf{u}_{\mathrm{A}} = (\bar{\mathbf{F}} - \mathbf{I})(\mathbf{X}_{\mathrm{B}} - \mathbf{X}_{\mathrm{A}}) \tag{2}$$

where A and B are two points periodically located on the boundary of the unit cell and $\bar{\mathbf{F}}$ is the macroscopic deformation gradient. Under equibiaxial compression, the macroscopic deformation gradient is given by $\bar{\mathbf{F}} = \lambda(\mathbf{e}_1 \otimes \mathbf{e}_1 + \mathbf{e}_2 \otimes \mathbf{e}_2)$. $\lambda$ is the macroscopically applied stretch and $\mathbf{e}_1$ and $\mathbf{e}_2$ are the basis vectors of two-dimensional Cartesian coordinates. Obviously, it can be noted that $\lambda = 1$, $\lambda > 1$, and $\lambda < 1$ represent the unstretched, extended, and compressed configurations, respectively. The primitive unit cells are shown in Figs. 2(*c*)–2(*e*). And the microscopic instability

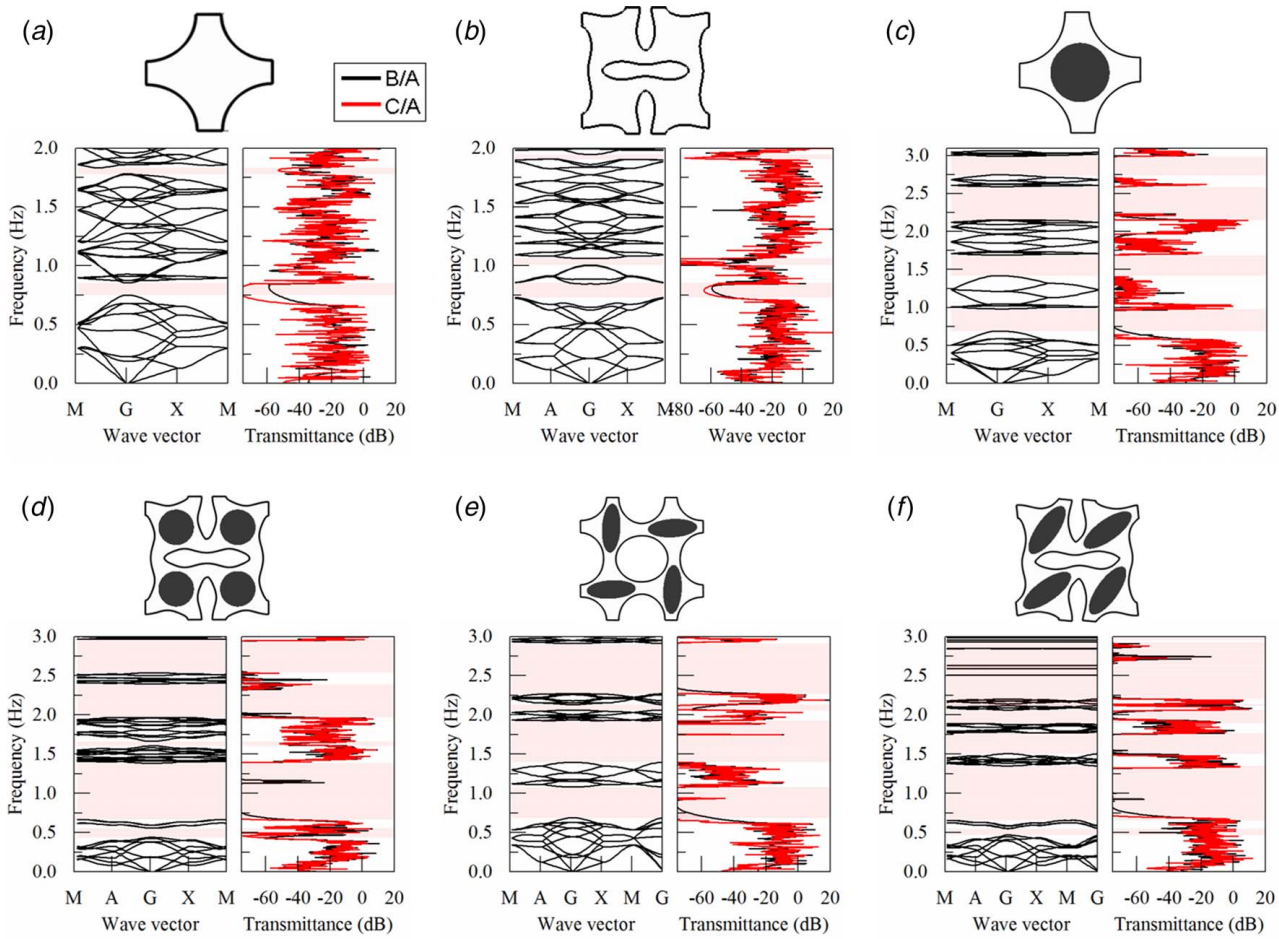


**Fig. 2 Unit cells and their band structures and transmittance spectrums. (*a*,*b*) Primitive and deformed configurations ($\lambda = 0.85$) under equibiaxial compression, and band structures of only pure periodic porous elastomeric matrices. (c)–(*f*) Primitive and deformed ($\lambda = 0.85$) configurations under equibiaxial compression, and band structures of PnCs with scatterers in periodic porous elastomeric matrices. (*c*,*d*) Cylindrical scatterer. (*e*,*f*) Elliptic cylinder scatterer. A denotes the measuring position of input, and B and C represent the measuring positions of output, respectively, as shown in Fig. 16 in Appendix A.**

leads to new unit cells shown in Figs. 2(*d*)–2(*f*). Also, as a contrast, the primitive and deformed unit cells of the pure periodic porous elastomeric matrix are shown in Figs. 2(*a*) and 2(*b*), respectively. For the primitive unit cells shown in Figs. 2(*a*)–2(*c*), the microscopic instabilities lead to an enlarged representative volume element of $2 \times 2$ primitive unit cells [48], as shown in Figs. 2(*b*)–2(*d*). In the post-buckling analysis, an imperfection in the form of the lowest eigenmode scaled by the scale factor $\eta$ ($\eta = 0.0005$) is introduced into the initial geometry by perturbing the position of each node.

Based on deformed configuration, the analysis of small amplitude elastic wave propagation will be performed. Here, to obtain the dispersion relation and to evaluate the directionality of the propagation waves in the PnCs, Bloch-type boundary conditions

$$\bar{\mathbf{u}}(\mathbf{x} + \mathbf{R}) = \bar{\mathbf{u}}(\mathbf{x}) \exp(i\mathbf{k} \cdot \mathbf{R}) \tag{3}$$

are applied to the edges of the unit cell, where $\bar{\mathbf{u}}$ and $\mathbf{x}$ denote the displacement and position vector of a point. $\mathbf{k}$ and $\mathbf{R}$ are the propagating Bloch-wave vector and the distance between each pair of nodes periodically located on the boundaries. By varying the value of $\mathbf{k}$ along the edges of the first irreducible Brillouin zone and solving the eigenvalue problem generated by the finite element method algorithm, the dispersion relations can be obtained. Also, we must note that the transformation of the irreducible Brillouin zone before and after deformation (see Fig. 1(*d*)). For example, for the undeformed unit cells shown in Figs. 2(*a*)–2(*c*), their irreducible Brillouin zones are the triangle zone GXM. For their deformed unit cells shown in Figs. 2(*b*)–2(*d*), their irreducible Brillouin zones are transformed to the rectangle zone MAGXM. Differently, for unit cells shown in Figs. 2(*e*) and 2(*f*), their irreducible Brillouin zones are the whole Brillouin zones MBDFM. It is not easy to accurately calculate its band structure, and the calculation is performed along the path MAGXMG. Meanwhile, to verify band gap's calculation accuracy, the transmittances of finite-sized PnC structures are calculated. The finite-sized PnC structure model is shown in Fig. 16 in Appendix A. The transmittance is defined as $T = 20\log_{10}(|u_{out}|/u_{in})$, where $u_{\text{in}}$ and $u_{\text{out}}$ are the displacements of the input and output positions. Also, the normalized frequency $\bar{f} = fl/c_t$, with $f$, $l$, and $c_t = 32.07$ m/s denoting the frequency, the characteristic size of the unit cell in the undeformed configuration, and the elastic wave speeds for shear wave in the matrix material, is adopted in this paper.

**2.2 Band Structures of PnCs Before and After Deformation.** Figure 2 shows the unit cells of PnCs before and after deformation and their band structures and transmittance spectrums. The scatterers have two forms of the cylindrical scatterer and elliptic cylinder scatterer with the ratio 2.667 of the semi-major axis and the semi-minor axis. They have the same cross-sectional area. The above subfigures in Figs. 2(*a*), 2(*c*), and 2(*e*) show the primitive unit cells of PnCs, and ones in Figs. 2(*b*), 2(*d*), and 2(*f*) show the new unit cells after deformation. For the unit cells shown in Figs.

2(*a*)–2(*c*), the microscopic instability leads to an enlarged unit cell consisting of 2 × 2 primitive unit cells, as shown in Figs. 2(*b*)–2(*d*).

Figures 2(*a*) and 2(*b*) show the band structures of the primitive and deformed configurations of pure periodic porous elastomeric matrix. Their band gaps are opened at 0.704–0.805 (12–13) and 1.729–1.78 (40–41) before deformation and at 0.731–0.859 (12–13), 1.005–1.064 (16–17), and 1.906–1.945 (44–45) after deformation, respectively. These band gaps are narrow. However, after embedding hard scatterers into the elastomeric matrix, the band gap characteristics of the PnCs are significantly enhanced. Taking the case of cylindrical scatterer shown in Figs. 2(*c*) and 2(*d*) as an example, the band gaps of PnCs are located at 0.691–0.983 (12–13), 1.420–1.692 (20–21), 2.152–2.594 (36–37), and 2.747–2.992 (44–45) in the undeformed configuration. However, in the deformed configuration ($\lambda = 0.85$), the pre-existing band gaps 0.691–0.983 (12–13) and 2.747–2.992 (44–45) are shifted and widened to 0.670–1.385 (12–13) and 2.539–2.966 (44–45); and the pre-existing band gaps 2.152–2.594 (36–37) is turned and narrowed to 1.967–2.395 (36–37). Also, two new band gaps are opened at 0.441–0.558 (8–9) and 1.606–1.665 (24–25). Differently, the PnCs showed in Figs. 2(*e*) and 2(*f*) take an elliptic cylinder as a scatterer. Similar to Figs. 2(*c*) and 2(*d*), it can be seen from Figs. 2(*e*) and 2(*f*) that the deformation significantly alters the band structures. The results of Figs. 2(*c*)–2(*f*) intuitively demonstrate that the geometrical shapes and the arrangement of scatterer can significantly affect the band structures of PnCs. Also, it can be seen from Fig. 2 that the band regions in the transmittance spectrums agree well with the predictions of band gaps in the band structures. In the band regions, the transmittances are significantly reduced so that the wave propagation in these frequency ranges are suppressed.

In short, we can manipulate the dynamic performances of PnCs through the deformation of the matrix. What should be more noticed is that the deformation can lead to the changes of geometrical shapes and material parameters (tangent modulus) of the matrix, the rearrangement of scatterers, the transformation of the coupling effect of holes in the matrix and multiple scatterers, and so on. In order to design new-style tunable PnCs, it is necessary to investigate how these changing factors induced by deformation affect the dynamic characteristics of PnCs.

## 3 Effect Factors of Manipulation of Dynamic Response of Phononic Crystal

Here, we will investigate the effects of these changing factors induced by deformation such as geometric and material nonlinearities, the rearrangement of scatterers and the coupling effect of holes and scatterers, on the dynamic characteristics of PnCs through calculating the band gaps of PnCs and the directionality of low-frequency wave propagation (group and phase velocities). Thus, the investigations will involve the following four aspects: the effect of coupling of holes and scatterers, the effect of geometric nonlinearity, the effect of material nonlinearity, and the effect of rearrangement of scatterers.

**3.1 Role of Coupling Effect of Holes and Scatterers.** Here, in order to evaluate the influence of the coupling effect of holes and scatterers on both the band structures, the geometric and material nonlinearities and the rearrangement of scatterers induced by deformation are not taken into consideration, and the primitive configurations of PnC with cylindrical scatterers are used to compute the dynamic response. It is assumed that the lattice length of the unit cell is 10 mm. According to the void volume fraction of 50.27% of circular holes and the filling rate of 18.85% of scatterers, the radius $R$ of the circular hole is 4 mm, and the radius $r$ of the cylindrical scatterer is 2.449 mm.

Figure 3(*a*) shows the evolution of the band gaps as a function of the radius $R$ of the circular hole, and Figs. 3(*b*) and 3(*c*) display the band structures of PnCs when the radiuses of the circular hole are 2.0 mm and 3.5 mm, respectively. It can be observed from Fig. 3(*a*) that there is only one band gap (1) when $R < 3.0$ mm and the position and width of the band gap remains nearly constant. However, when $R > 3.0$ mm, new band gaps (2 and 3) are opened. With the increase of the radius $R$ of the circular hole, the coupling effect of holes and scatterers is enhanced. The positions of new band gaps alter, and especially their widths increase with the increase of radius $R$ of the circular hole.

Figure 4 shows the evolution of the band gaps as a function of the radius $r$ of the cylindrical scatterer. Figures 4(*b*) and 4(*c*) exhibit the band structures of PnCs when the radiuses of the cylindrical scatterer are 1.225 mm and 2.143 mm, respectively. It can be observed from Fig. 4 that the position and width of the first band gap (1) keep constant when $r < 1.5$ mm. However, when $r > 1.5$ mm, other band gaps (such as 2 and 3) are opened. With the increase of radius $r$ of the cylindrical scatterer, the coupling effect of holes and scatterers is also enhanced, and the positions of new band gaps shift to high-frequency, and their widths increase.

The relative size of the circular hole and cylindrical scatterer determines the extent of the coupling effect. It can be gotten from Figs. 3(*a*) and 4(*a*) that only when $r > 1.5$ mm ($R = 4.0$ mm) or $R > 3.0$ mm ($r = 2.449$ mm) new band gaps (such as 2 and 3) are opened. Namely, the strong coupling effect of hole and scatterer contributes to the formation of band gaps, and it is one of the key design parameters of PnC. In addition, in Appendix B, the effects of the cross-sectional size of the cylinder, the ratio semi-major axis and semi-minor axis of elliptical cylinders, and the arrangement of scatterer on the critical applied stretch of instability are investigated, as shown in Fig. 17. These results indicate different geometrical sizes and shapes of scatterers can alter the critical applied stretch of the instability of unit cells of PnCs, and thus

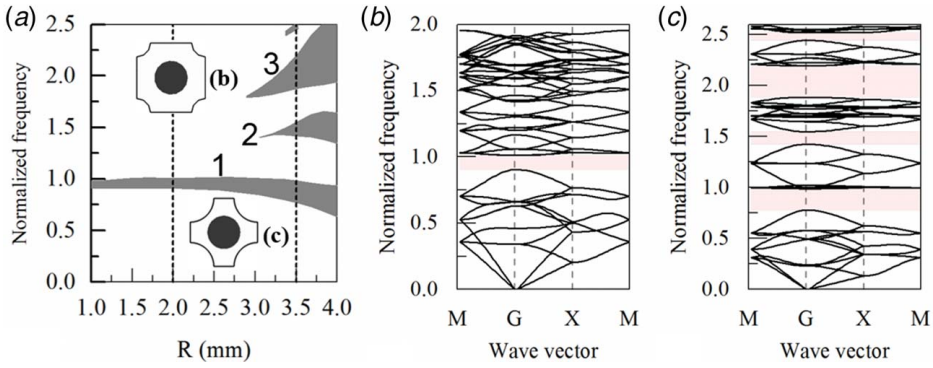


**Fig. 3 (*a*) The evolution of the band gaps as a function of the radius *R* of the circular hole. (*b,c*) The band structures when the radiuses of the circular hole are 2.0 mm and 3.5 mm, respectively. The numbers denote the serial numbers of band gaps.**

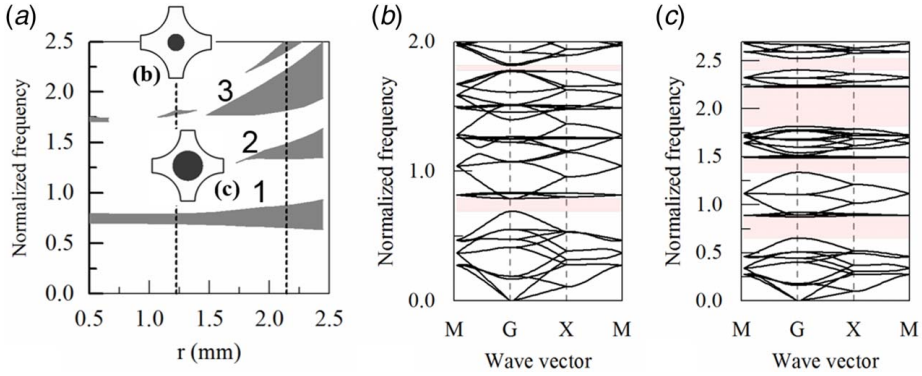


**Fig. 4 (*a*) The evolution of the band gaps as a function of the radius *r* of the cylindrical scatterer. (*b*,*c*) The band structures when the radiuses of cylindrical scatterer are 1.225 mm and 2.143 mm, respectively. The numbers denote the serial numbers of band gaps.**

they can also be used to design composites of different mechanical properties.

**3.2 Role of Geometric Nonlinearity of Matrix.** Next, to evaluate the effect of geometric nonlinearity on the dynamic response of the PnCs, the PnC with cylindrical scatterers is still designed to exclude the effect of rearrangement of scatterers. And the deformed geometrical shape of the structure determined by the post-buckling is used to investigate the propagation of elastic waves. In addition, to exclude the effect of stress, all the components of the stress are set to zero before performing the wave propagation analysis.

Figure 5(*a*) shows the evolution of the band gaps as a function of $\lambda$. Red dot-dash lines in Fig. 5(*a*) represent the band gaps of PnCs with considering stress distribution. In this figure, the blue numbers denote the serial numbers of band gaps. It can be observed that during deformation, the second (2) and seventh (7) band gaps shift and widen, but the third (3) and sixth (6) ones shift and narrow, and the third (3) one even vanishes, and the first (1), fourth (4), and fifth (5) ones are opened at $\lambda = 0.94$, $\lambda = 0.89$, and $\lambda = 0.98$, respectively. Figure 5(*b*) shows the band structures of PnCs in the deformed configurations (left figure: $\lambda = 0.925$ and right figure: $\lambda = 0.85$). They intuitively exhibit the effect of geometric nonlinearity on band structures. These results demonstrate that the geometric nonlinearity plays an important role in the manipulation of dynamic characteristic of PnC through deformation. In addition, the differences between with (Fig. 2(*c*)) and without (Fig. 5(*b*)) considering stress distributions indicate that the material nonlinearity can significantly alter the dynamic characteristic of high-frequency range.

Unlike the calculation process of band structures along the boundary paths of irreducible Brillouin zones, solving with respect to frequency for all the combination $\mathbf{k} = (k_x, k_y)$ in the whole Brillouin zones yields a series of functions $\omega = f(k_x, k_y)$, denoted as phase constant surface (PCS), which identifies the frequency of free wave motion for any given $(k_x, k_y)$ pair [51]. For example, Fig. 6 shows the first two PCSs of PnCs before and after deformation ($\lambda = 1.0$ and $\lambda = 0.85$), respectively. They provide the wavenumber-frequency information in the whole Brillouin zones. The PCS can provide rich information about the wave propagation characteristics of interested frequency ranges through PCS. Based on PCS, The phase and group velocities can be defined as

$$\mathbf{c}_p = \frac{\omega}{\mathbf{k}}, \quad \mathbf{c}_g = \frac{\partial \omega}{\partial \mathbf{k}} \tag{4}$$

For the undamped structures, the group velocity reflects the propagation velocity of the wave energy and the propagation direction of the wave energy. Usually, the direction of wave propagation is perpendicular to a given iso-frequency plot of PCS [52]. In this way, we can investigate the directionality of the wave propagation in the PnCs before and after deformation at a specific frequency. Further, in order to evaluate the degree of anisotropy of the undeformed and deformed configurations, the formulation of the

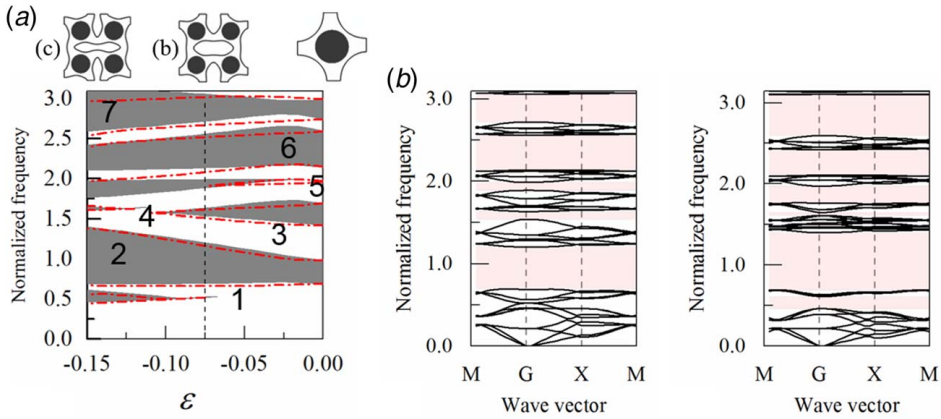


**Fig. 5 (*a*) The evolution of the band gaps as a function of $\lambda$ under equibiaxial compression. The numbers denote the serial numbers of band gaps. (*b*,*c*) The band structure for the deformed configurations (left, $\lambda = 0.925$; right, $\lambda = 0.85$). Dot-dash lines in (*a*) represent the band gaps of PnCs with considering stress distribution.**

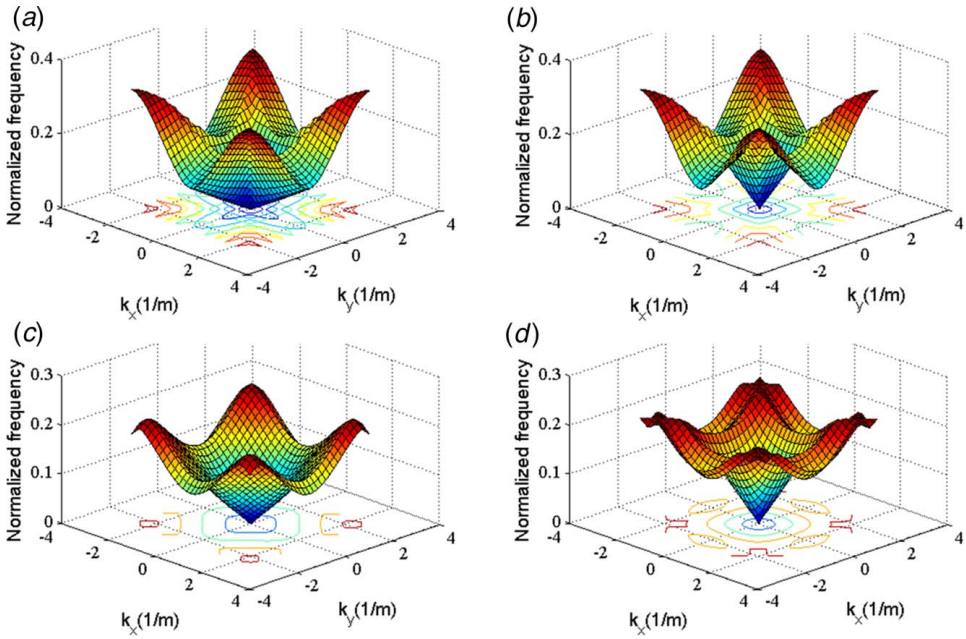


**Fig. 6 Phase constant surface. (*a*,*b*) The primitive configuration ($\lambda = 1.0$) and (*c*,*d*) the deformed configuration ($\lambda = 0.85$). (*a*) and (c): mode 1; (*b*) and (*d*): mode 2.**

anisotropy index (*AI*) is defined as [53]

$$AI = \sqrt{\int_0^{2\pi} \left[\frac{c_g(\theta) - \bar{c}_g}{\bar{c}_g}\right]^2 d\theta} \tag{5}$$

where $c_g(\theta)$ denotes the magnitude of the group velocity relative to a certain mode as a function of the angular position $\theta$, and $\bar{c}_g$ is the average value of $c_g(\theta)$ over the full 360 deg angular range, namely

$$\bar{c}_g = \frac{1}{2\pi}\int_0^{2\pi} c_g(\theta) d\theta \tag{6}$$

From the formulation of *AI*, it can be noted that $AI = 0$ defines the isotropic case, and a structure having $AI \neq 0$ is characterized by a certain degree of anisotropy. From Fig. 6, the iso-frequency contours can be gotten, as shown in Fig. 7. Figure 7 shows the iso-frequency contours of the first two PCSs when the applied stretches are $\lambda = 1.0$, $\lambda = 0.925$ and $\lambda = 0.85$ at $\bar{f} = 0.078$ (corresponds to the real frequency 250 Hz). Correspondingly, Figs. 8(*a*) and 8(*b*) display their group velocity profiles. It can be observed from Figs. 6 and 7 that in the undeformed configuration, the iso-frequency contours of the first two PCSs display significant anisotropy, and with the decrease of the applied stretch $\lambda$ (corresponds to the increase of compressive deformation), the iso-frequency contours tend to circle. Meanwhile, as shown in Figs. 8(*a*) and 8(*b*), the directionalities of group velocity have significant changes with the decrease of the applied stretch $\lambda$. For example, in the undeformed configuration, the group velocity exhibits two preferred directions at about 5 deg and 85 deg for the first two PCSs at $\bar{f} = 0.078$, and the corresponding AIs are 0.820 and 0.336. In the deformed configuration ($\lambda = 0.85$), the preferred directions of group velocity for the first PCS at $\bar{f} = 0.078$ changes to about 45 deg and the corresponding AI is 0.136. However, for the second PCS, there is no significant preferential direction, and the corresponding AI is 0.087. Figure 10(*c*) exhibits the evolution of the AI as a function of applied stretch $\lambda$. It can be seen that with

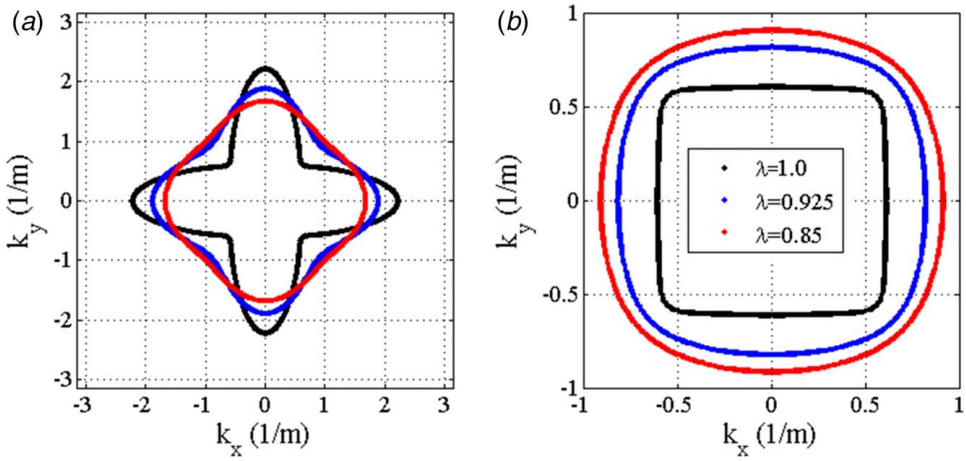


**Fig. 7 Iso-frequency ($\bar{f} = 0.078$, which corresponds to the real frequency 250 Hz) contours of the first two PCSs for the PnCs with different stretch as $\lambda = 1.0$, $\lambda = 0.925$, and $\lambda = 0.85$: (*a*) the first PCS and (*b*) the second PCS**

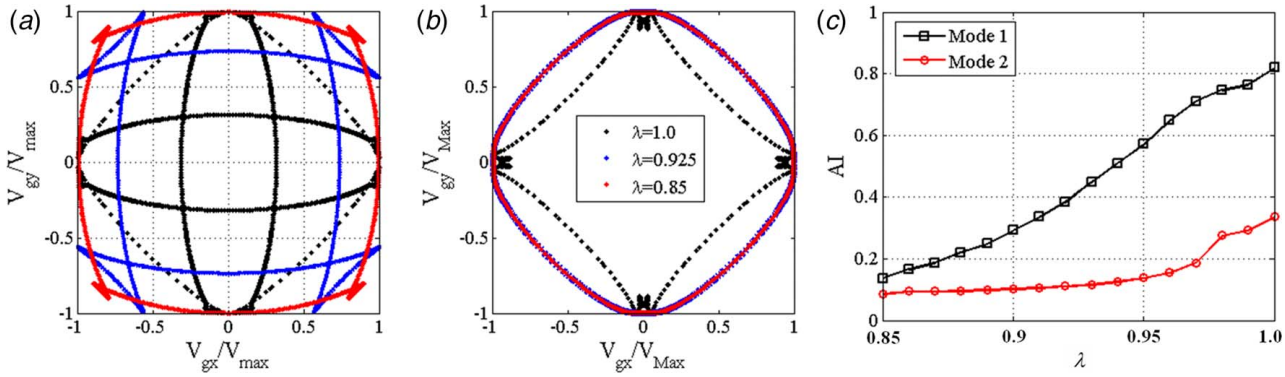


**Fig. 8 Effects of deformation ($\lambda = 1.0$, $\lambda = 0.925$, and $\lambda = 0.85$) on the directionality of group velocities: (*a*) mode 1, (*b*) mode 2, and (*c*) variations of anisptropy index of the first two modes of tunable PnCs with respect to the applied stretch $\lambda$ at $\bar{f} = 0.078$ with corresponding to the real frequency 250 Hz.**

the decrease of applied stretch $\lambda$, the AI decreases and tends to zero, which means that the deformed PnC behaves as a nearly isotropic medium with a decrease of deformation. In summary, the geometrical deformation of mechanically tunable PnC can realize the manipulation of band gaps, while it makes the deformed PnC to behave as a nearly isotropic medium so that the directionality of wave propagation disappears.

**3.3 Role of Material Nonlinearity of Matrix.** During compression, the stress distributions within the PnCs significantly vary, and they can affect the dynamic response of PnCs. The stress distributions are closely related to the material nonlinearity. Here, in order to investigate the effect of material nonlinearity on the band structures and wave directionality, an almost-incompressible elastomeric material whose response is captured by a Gent model is used to make the PnCs [35,54]. The Gent model is characterized by the following strain energy density function:

$$W(I_1, J) = -\frac{\mu}{2} J_m \log\left(1 - \frac{I_1 - 3}{J_m}\right) - \mu \log(J) + \left(\frac{\kappa}{2} - \frac{\mu}{J_m}\right)(J-1)^2 \tag{7}$$

where $I_1 = \text{trace}(\mathbf{F}^T\mathbf{F})$, $J = \det(\mathbf{F})$, $\mathbf{F}$ denotes the deformation gradient and $J_m$ denotes a material constant related to the strain at saturation. The initial shear ($\mu$) and bulk ($\kappa$) moduli use the same the parameters as mentioned above. Note that as $J_m \to +\infty$ the Gent model reduces to the Neo-Hookean model and the smaller value of $J_m$ introduces stronger nonlinearity in the material behavior [35]. Similarly, to exclude the effect of the arrangement of the scatterer, the cylindrical scatterer is chosen to design the PnCs. Figure 9 shows the evolution of the band gaps as a function of the applied stretch $\lambda$ for the PnCs with $J_m = 1.0$, 5.0 and $\infty$, respectively. Red dot-dash lines represent the band gaps of PnCs with the Neo-Hookean model. It can be seen from Fig. 9 that the stronger nonlinearity of matrix material can enhance the tenability of the band gap. In order to clearly display the effect of the material parameter $J_m$ on the band gaps, the relative size $\delta$ of the band gap as the ratio between gap width and the midgap position is defined as [35]

$$\delta = \frac{f_{up} - f_{low}}{(f_{up} + f_{low})/2} \tag{8}$$

where $f_{up}$ and $f_{low}$ are the frequencies of upper and lower edge limits of a band gap, respectively. The evolution of $\delta$ as a function of the applied stretch $\lambda$ is exhibited in Fig. 10 for the band gaps shown in Fig. 9. Note that the relative size $\delta$ of the band gaps marked by the blue dashed rectangle in Fig. 9 is not shown in Fig. 10. In addition, the solid purple lines ($J_m = \infty$, Geom.) in Fig. 10 indicate the relative size $\delta$ of the band gaps shown in Fig. 5(*a*), whose stress distribution is not considered. The differences between them indicate the stress distributions can significantly affect the dynamic responses of PnCs.

Here, the PnCs with Gent material models of $J_m = 1.0$, 5.0, 10.0, and $\infty$ (corresponds to Neo-Hookean model) are considered. It can be observed from Fig. 10 that the relative sizes $\delta$ of the band gaps significantly vary with the decrease of the applied stretch $\lambda$. The variation of the relative size $\delta$ reflects the relative variation of the position and width of the band gap during deformation. For example, in Fig. 9, the positions and widths of the first (1, 8–9) and second (2, 12–13) band gaps increase with the decrease of the applied stretch $\lambda$, and their relative sizes $\delta$ shown in Figs. 10(*a*) and 10(*b*) monotonically increase, which indicates the widening value is stronger than the position shifting value. For another example, Fig. 10(*e*) exhibits

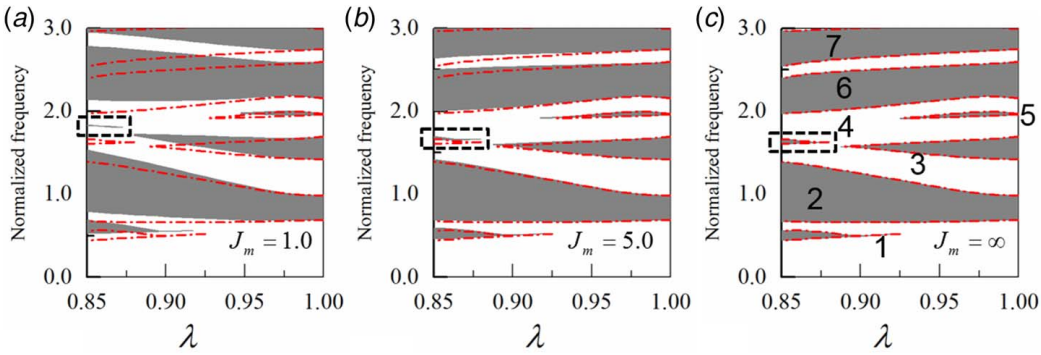


**Fig. 9 The evolution of the band gaps as a function of $\lambda$ for the different material parameter $J_m$: (*a*) $J_m = 1.0$, (*b*) $J_m = 5.0$, and (*c*) $J_m = \infty$ (or Neo-Hookean model). Dot-dash lines represent the band gaps of PnCs with Neo-Hookean model. The blue numbers denote the serial numbers of band gaps.**

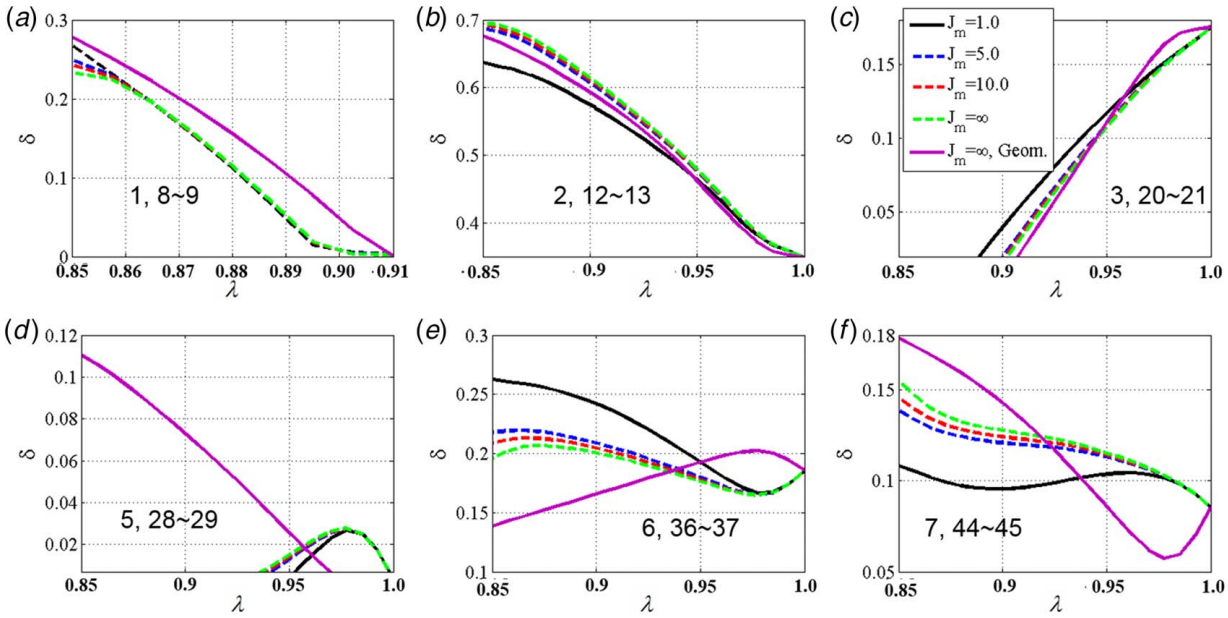


**Fig. 10** Comparison of the relative parameter $\delta$ of the band gaps during deformation. $n_i \sim n_j$ denotes the numbers of the upper and lower edge modes of a band gap. Except the band gap (4, 24–25) indicated by the red dashed rectangle in Fig. 9, the relative parameters $\delta$ for other band gaps from bottom up are shown in (*a*)–(*f*), respectively. The numbers denote the serial numbers of band gaps.

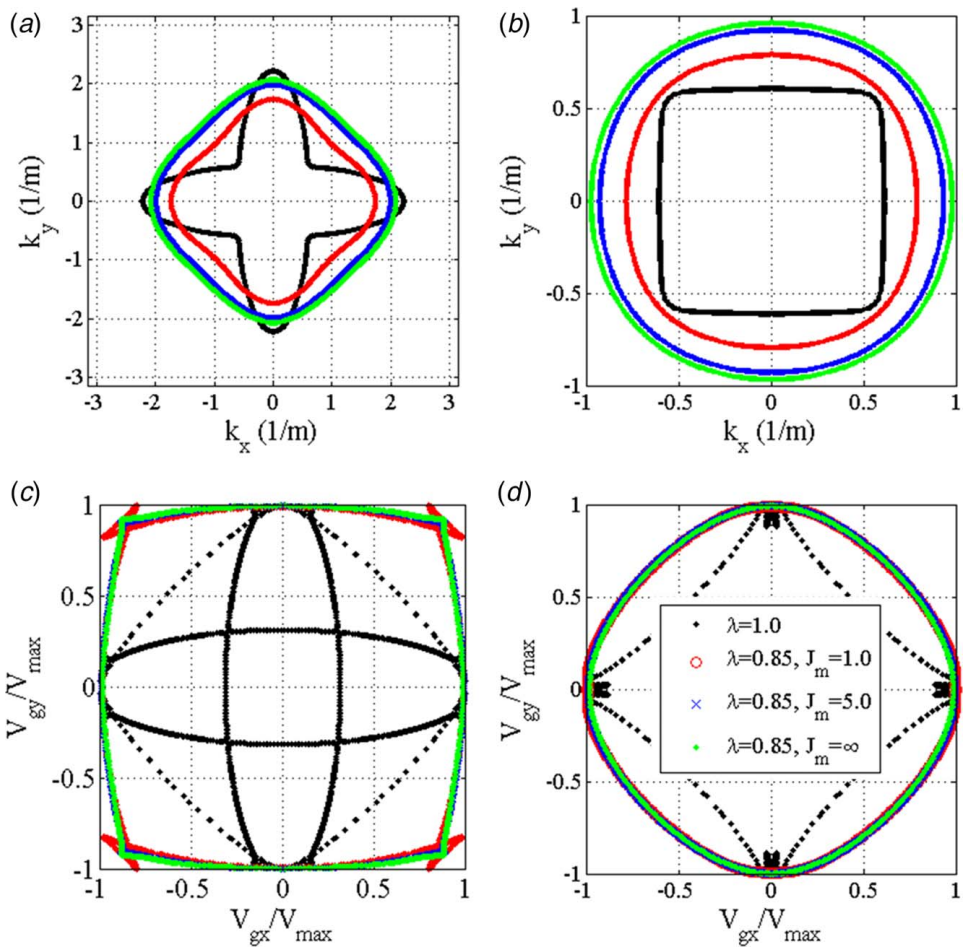


**Fig. 11** Iso-frequency ($\bar{f} = 0.078$, which corresponds to the real frequency 250 Hz) contours of the first two PCSs of the PnCs with different material parameters $J_m = 1.0$, 5.0, and $\infty$, and effects of material parameters on the directionality of group velocities before and after ($\lambda = 0.85$) deformation. (*a*,*b*) The iso-frequency contours of the first two PCSs at $\bar{f} = 0.078$; (*c*,*d*) the corresponding directionality of group velocities; (*a*,*c*) for the first PCS; (*b*,*d*) for the second PCS.

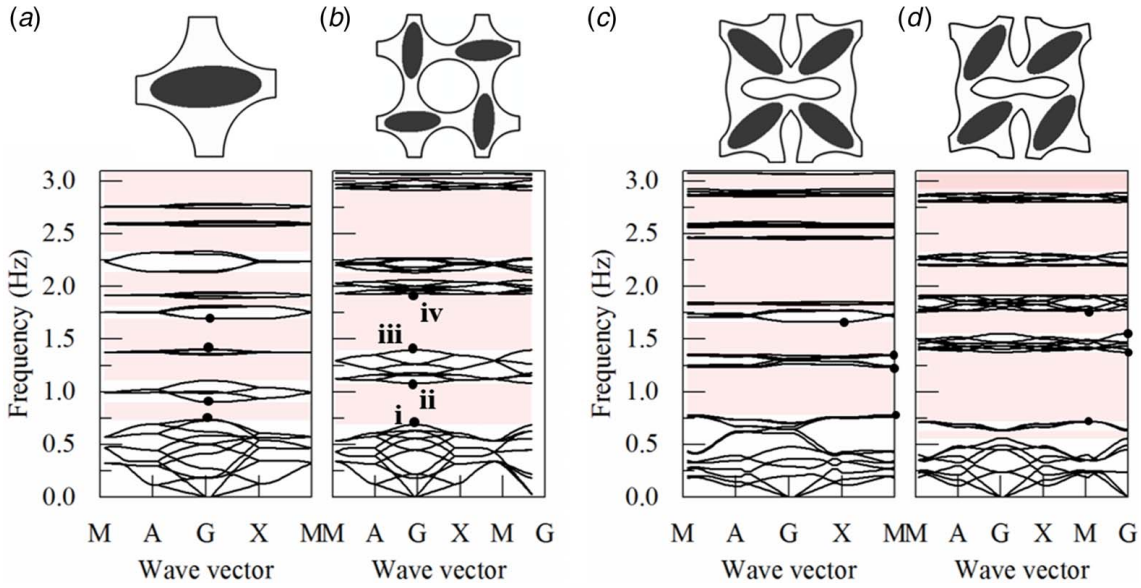


**Fig. 12 Band structures of the PnCs with scatterers of different arrangement in the deformed configurations ($\lambda = 0.85$). (*a*,*b*) Primitive configurations and (*c*,*d*) deformed configurations. (*c*) The deformed configuration of (*a*), and (*d*) the deformed configuration of (*b*). The PnCs in (*a*,*c*) and (*b*,*d*) are marked as Ellipse-A and Ellipse-B, respectively. The points denote the mode frequencies of choice and their Bolch mode shapes are shown in Fig. 18 in Appendix C. These points from low to high are marked as i, ii, iii, and iv, respectively. Points i, ii, iii, and iv correspond to modes 12, 13, 20, and 21, respectively.**

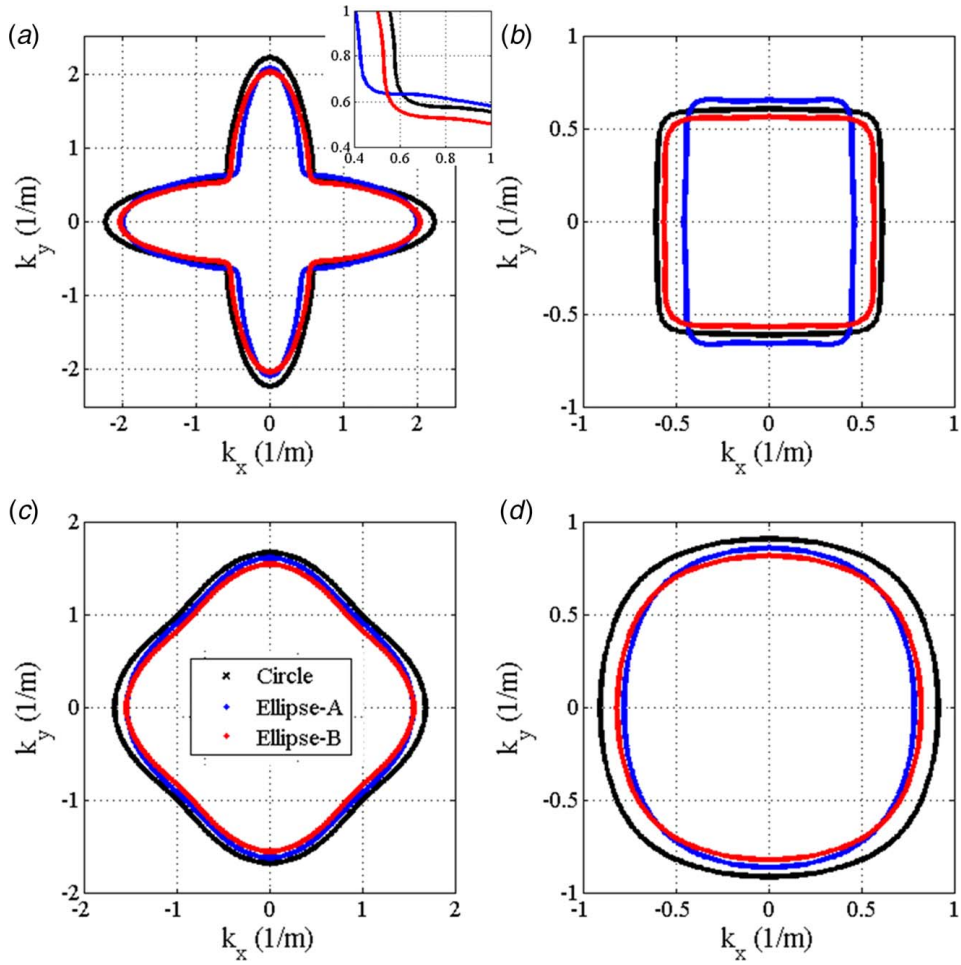


**Fig. 13 Iso-frequency ($\bar{f} = 0.078$ with corresponding to the real frequency 250 Hz) contours of the first two PCSs of the PnCs with scatterers of different geometry and arrangement before and after deformation. (*a*,*b*) The first PCS, (*c*,*d*) the second PCS, (*a*,*c*) before deformation, and (*b*,*d*) after deformation ($\lambda = 0.85$).**

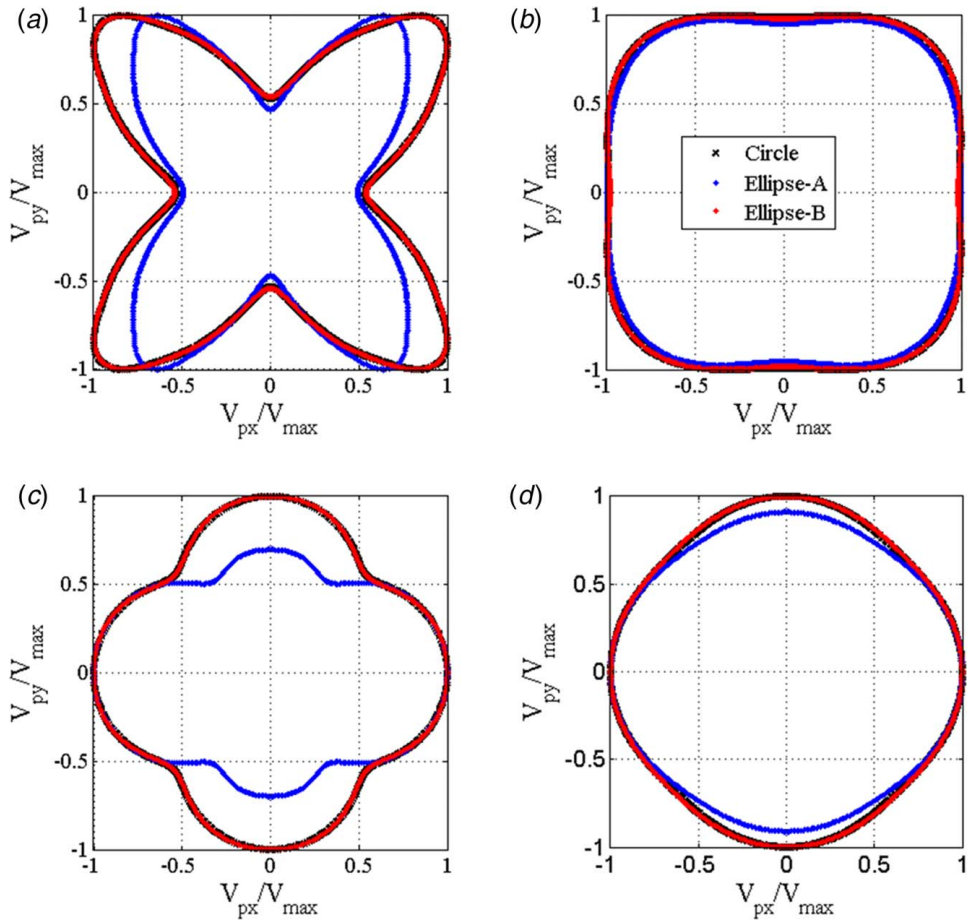


**Fig. 14 Effects of geometry and arrangement of scatterers on the directionality of phase velocities at $\bar{f} = 0.078$ (corresponds to the real frequency 250 Hz) for primitive ((*a*) and (*c*), $\lambda = 1.0$) and deformed ((*b*) and (*d*), $\lambda = 0.85$) configurations. (*a,b*) the first PCS and (*c,d*) the second PCS.**

that the relative size $\delta$ of the sixth band gap (6) shown in Fig. 9 first decreases and reaches a minimum at about $\lambda = 0.975$, and then increases and reaches a maximum and finally decreases, which reflects the complex change process of the sixth band gap. It can be clearly observed from Figs. 9 and 10 that the band gaps of PnCs with different material parameter $J_m$ and their relative sizes $\delta$ have notable differences. Especially, the PnC with stronger material nonlinearity (for example $J_m = 1.0$) has much stronger tunability of band gap.

In order to investigate the effect of material nonlinearity on the directionality of wave propagation, Fig. 11 shows the iso-frequency contours of the first two PCSs and the corresponding group velocity profiles at $\bar{f} = 0.078$ (corresponds to the real frequency 250 Hz) before and after deformation. Here the PCSs are similar to those shown in Fig. 6 and are not repeated here. First, it can be seen from Fig. 11(*a*) that although the matrix of PnCs is made of elastomeric material with different parameters $J_m = 1.0$, 5.0, and $\infty$, the iso-frequency contours of the first two PCSs and their group velocity profiles almost have the same shapes. The anisotropy indexes of the first PCS are 0.195, 0.176, and 0.187, and those of the second PCS are 0.069, 0.061, and 0.062 at $\bar{f} = 0.078$ for the matrix material with $J_m = 1.0$, 5.0, and $\infty$, respectively. These results indicate the material nonlinearities do not affect the directionality of the wave propagation. In short, the stronger nonlinearity of material can enhance the tunability of the band gap, but it cannot affect the directionality of wave propagation in the PnCs.

**3.4 Role of Rearrangement of Scatterers During Deformation.** We have known that rotating the scatterers with geometric anisotropy can be used to tune the dynamic response of PnCs [43]. However, this strategy is feasible only when the matrix material is gas or liquid. In this paper, we propose that the rearrangement of scatterers of solid-solid PnCs can be controlled through the deformation of the matrix structure. During deformation, the effect of the rearrangement of scatterers on the dynamic response of PnCs couples with the geometric and material nonlinearities. Here, to evaluate the impact of rearrangement of scatterers, all the stress components are set to zero before performing the wave propagation analysis. Here, the PnCs with scatterers of two kinds of arrangement are designed to investigate the elastic waves' propagation, as shown in Fig. 12. The scatterers are arranged according to Figs. 12(*a*) and 12(*b*), which are, respectively, marked as Ellipse-A and Ellipse-B, and Figs. 12(*c*) and 12(*d*) show their deformed configurations ($\lambda = 0.85$).

Figures 12(*a*) and 12(*b*) shows the band structures of PnCs in the primitive configurations. The result in Fig. 12(*b*) is the same in Fig. 2(*e*). For comparison, it is repeated here. The differences between Figs. 12(*a*) and 12(*b*) demonstrate that the rearrangement of scatterers significantly alters the band structures of PnCs. Figures 12(*c*) and 12(*d*) display the band structures of PnCs in the deformed configurations ($\lambda = 0.85$). In comparison with Figs. 12(*a*) and 12(*b*), it can be seen from Figs. 12(*c*) and 12(*d*) that the band structures of PnCs in the deformed configuration are different from those in the undeformed configuration. For example, there are eight and four band gaps in the undeformed configuration in Figs. 12(*a*) and 12(*b*), respectively. And there is no band gap between the 36th and 37th modes in Fig. 12(*a*), but in Fig. 12(*b*), the band gap between the 36th and 37th modes is opened at 2.271–2.911. In the deformed configuration ($\lambda = 0.85$), the band

gap between the 12th and 13th modes is opened at 0.783–1.236 in Fig. 12(*c*), but in Fig. 12(*d*), the corresponding band gap is opened at 0.719–1.377. Further, the mode shapes at these points marked by red points in Fig. 12 are shown in Fig. 18. Their mode shapes have significant differences in the same modes. These differences are caused by the difference in the scatterers' arrangement, which leads to the difference in band structures and band gaps of PnCs. In summary, the results of Fig. 12 demonstrate the rearrangement of scatterers plays an essential role in forming of band gaps. Because the band structure of PnC in Fig. 2(*f*) considers the effect of stress distribution, the differences between Figs. 12(*d*)–2(*f*) also reflect the impact of material nonlinearity on the band structures of PnCs.

Next, the effects of the rearrangement of scatterers on the directionality of wave propagation will be investigated. Figure 13 shows the iso-frequency contours of the first two PCSs of the PnCs before and after deformation. Their PCSs are similar to those shown in Fig. 6. It can be observed from Fig. 13 that the iso-frequency contours of the PnCs marked as circle and Ellipse-B have identical shapes, and they are different from that of the PnC marked as Ellipse-A at $\bar{f} = 0.078$. Figures 14 and 15 exhibit the corresponding phase and group velocity profiles in the undeformed and deformed configurations ($\lambda = 0.85$), respectively. It can be observed that that the phase and group velocities of the PnCs marked as circle and Ellipse-B have almost the same profiles, and they are different from those of the PnC marked as Ellipse-A.

For the PnCs marked as circle and Ellipse-B, it can be observed from Figs. 14(*a*), 14(*c*), 15(*a*), and 15(*c*) that they exhibit some preferred directions of wave propagation before deformation. After deformation, the preferred directions of wave propagation vanish, as shown in Figs. 14(*b*), 14(*d*), 15(*b*), and 15(*d*). To quantify the changes of direction of wave propagation, Table 1 lists the anisotropy indexes based on phase and group velocities before and after deformation at $\bar{f} = 0.078$, respectively. The anisotropy index

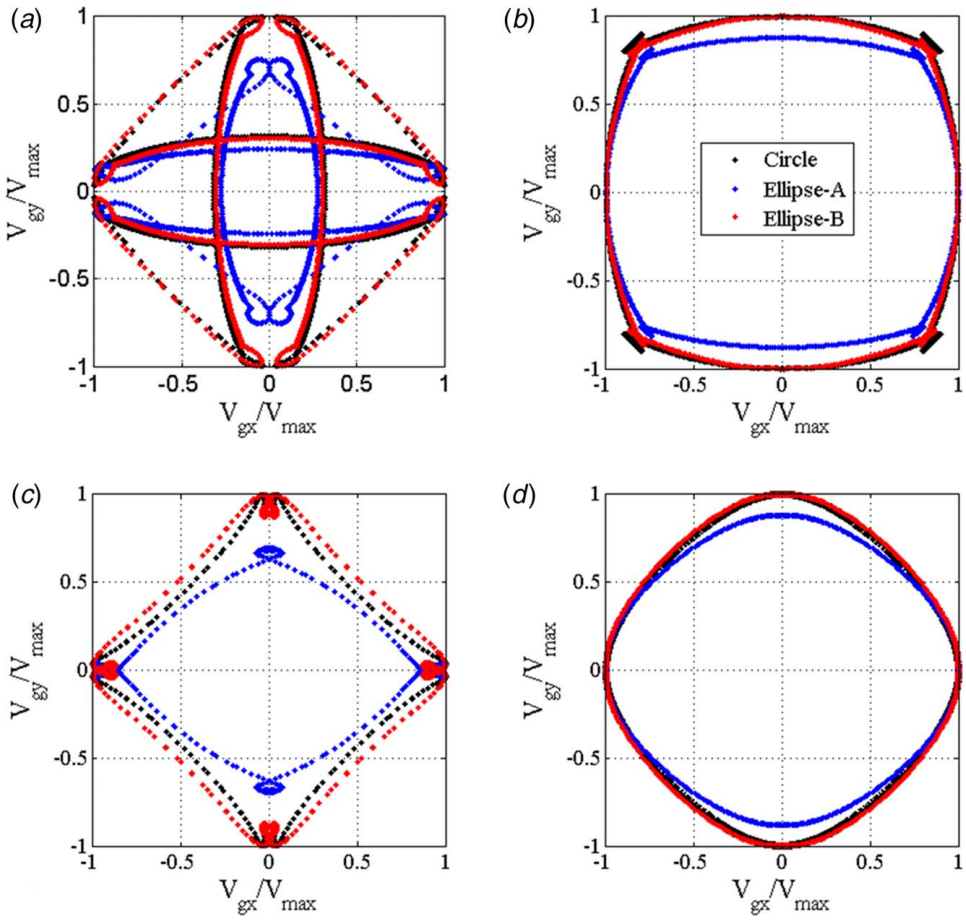


**Fig. 15 Effects of geometry and arrangement of scatterers on the directionality of group velocities at $\bar{f} = 0.078$ (corresponds to the real frequency 250 Hz) for primitive ((*a*,*c*), $\lambda = 1.0$) and deformed (*b*,*d*), $\lambda = 0.85$) configurations. (*a*,*b*) The first PCS and (*c*,*d*) the second PCS.**

**Table 1 Anisotropy indexes based on phase and group velocities of PnCs with scatterers of different geometry and arrangement**

| | Anisotropy index based on phase velocity | | | | Anisotropy index based on group velocity | | | |
|---|---|---|---|---|---|---|---|---|
| | Mode 1 | | Mode 2 | | Mode 1 | | Mode 2 | |
| | Fig. 14(*a*) | Fig. 14(*b*) | Fig. 14(*c*) | Figure 14(*d*) | Fig. 15(*a*) | Figure 15(*b*) | Fig. 15(*c*) | Figure 15(*d*) |
| Circle | 0.760 | 0.153 | 0.209 | 0.063 | 0.820 | 0.136 | 0.336 | 0.087 |
| Ellipse-A | 0.748 | 0.140 | 0.446 | 0.103 | 0.872 | 0.166 | 0.328 | 0.132 |
| Ellipse-B | 0.751 | 0.158 | 0.214 | 0.055 | 0.844 | 0.115 | 0.264 | 0.075 |

based on phase velocity can be calculated by Eqs. (6) and (7), where $c_g$ need to be replaced by $c_p$ [52,53]. It can be noted from Table 1 that the anisotropy indexes based on phase and group velocities for the PnCs marked as Circle and Ellipse-B are in good agreement. After deformation, the anisotropy indexes tend to zero, which indicates that the PnCs tend to be a nearly isotropic medium after deformation.

For the PnC marked as Ellipse-A, it can be seen from Figs. 14(*a*), 14(*c*), 15(*a*), and 15(*c*) that before deformation, the maximum of phase and group velocities in *X*-direction are different from those in *Y*-direction. Thus, the directional characteristic of the wave propagation in the *X*-direction is different from that in *Y*-direction. After deformation, the differences between the directional characteristics in *X*- and *Y*-directions decrease, as shown in Figs. 14(*b*), 14(*d*), 15(*b*), and 15(*d*). The deformed PnCs tend to be a nearly isotropic medium, verified by its anisotropy indexes listed in Table 1. However, it can still be observed that its phase and group velocities have obvious differences from those of the PnCs marked as Circle and Ellipse-B. The differences are due to the effect of the rearrangement of scatterer on the directionality of wave propagation.

In short, the PnCs with scatterers of different arrangement can realize various dynamic characteristics. Significantly, the rearrangement of scatterers induced by deformation can simultaneously manipulate the band gaps of PnCs and the directionality of wave propagation in them.

## 4 Discussion and Conclusions

The solid–solid PnCs comprised multiple scatterers and periodic porous elastomeric matrix can realize the band gaps' manipulation and the directionality of wave propagation in them through deformation. In this paper, the impacts of some tunable factors induced by deformation, such as the coupling effect of scatterers and holes, geometric and material nonlinearities, and the rearrangement of scatterers, on the formation of the band gap and the directionality of wave propagation in the PnCs are investigated. The following conclusions have been obtained:

The relative sizes of scatterer and hole in the matrix determine their coupling effect. The formation of band gaps needs their relative sizes to reach a certain extent. The strong coupling effect between them more contributes to the formation of band gaps. The geometric and material nonlinearities of the matrix induced by deformation can achieve the manipulation of band gaps. However, the directionality of wave propagation is only sensitive to the changes in geometry. The rearrangement of scatterers in the PnCs induced by deformation can simultaneously manipulate the band gaps of PnCs and the directionality of wave propagation in them. Significantly, the geometry deformation of the matrix makes the wave propagation more isotropic in the low-frequency range. In short, the tunability of the dynamic characteristic of PnC is the result of the comprehensive function of these tunable factors mentioned above.

In fact, besides the effect factors mentioned above, other issues are considered in the application, such as viscous/damping effects and manufacturing feasibility. The soft material is usually selected as the matrix material to enhance the tunability and reusability, but its intrinsic damping characteristic significantly influences the wave propagation into the PnCs. Recently, some research works have been considered the influence of viscous/damping effect on the dynamic responses of PnCs [37,55–57]. The impact of the viscous/damping effect on PnCs and acoustic metamaterials is crucial for exact predictions of the wave propagation performances, which should be considered in the application.


## Acknowledgment

This work is supported by the Science Challenge Project, No. TZ2018002, National Natural Science Foundation of China under Grant Nos. 11972205 and 11722218, the National Key Research Development Program of China (No. 2017YFB0702003), and Tsinghua University Initiative Scientific Research Program.


## Conflict of Interest

There are no conflicts of interest.

## Data Availability Statement

The datasets generated and supporting the findings of this article are obtainable from the corresponding author upon reasonable request. The authors attest that all data for this study are included in the paper. No data, models, or code were generated or used for this paper.

## Appendix A

Figure 16 shows the finite-size PnC structures. The scatterer can be replaced by those shown in Fig. 2. Letter A denotes the measuring position of input, and letters B and C represent the measuring output positions, respectively. The in-plane load is applied at position A.

## Appendix B

Figure 17 shows the evolution of the first two critical applied stretches $\lambda$ versus the geometrical parameters of hard scatterers. In this figure, $R_0$ is the radius of a cylinder with a filling rate of 18.85% and $\alpha_i$ is a proportionality coefficient. Here, we investigate the effects of the cross-sectional dimensions of the cylinder and elliptical cylinder on the first two critical applied stretches $\lambda$. For the cylinder, the cylinder's radius is controlled by $R = R_0\alpha_i$. The sectional area of the cylinder increases with the increase of proportionality coefficient $\alpha_i$. For the elliptical cylinder, its sectional area keeps constant, and its sectional geometric is controlled by the

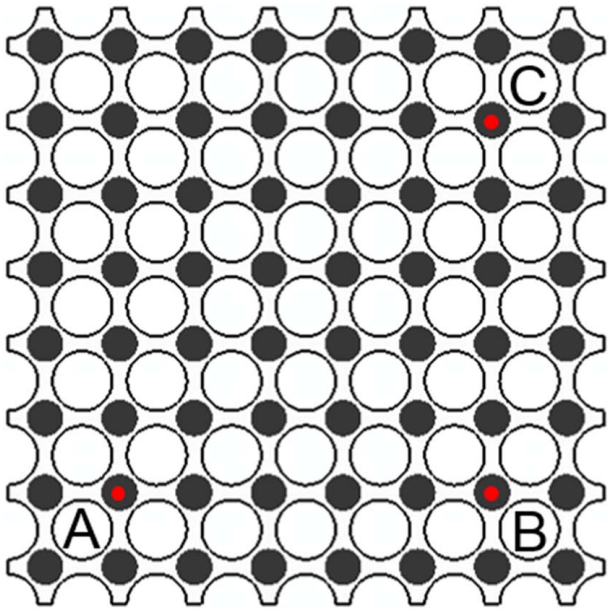


**Fig. 16 Finite-size PnC structure model. Letter A denotes the measuring position of input, and letters B and C denote the measuring positions of output, respectively. The scatterer can be replaced by those shown in Fig. 2.**

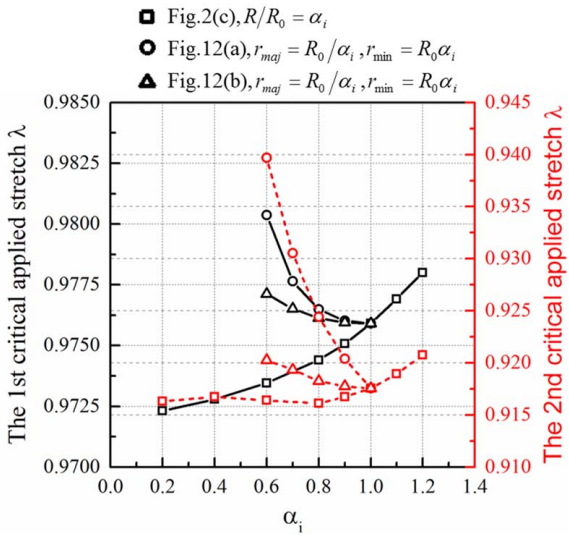


**Fig. 17 Evolution of the first two critical applied stretches $\lambda$ versus the geometrical parameters of hard scatterers. $R_0$ is the radius of cylinder with a filling rate 18.85% and $\alpha_i$ is a proportionality coefficient.**

ratio of semi-major axis and semi-minor axis. The lengths of the semi-major and semi-minor axes are $r_{maj} = R_0/\alpha_i$ and $r_{min} = R_0\alpha_i$, respectively. Two arrangements of the elliptical cylinder, as shown in Figs. 12(*a*) and 12(*b*), are considered. As the proportionality coefficient $\alpha_i$ approaches 1, the cross section of an elliptical cylinder tends to circle. It can be seen from Fig. 17 that the critical applied stretches are closely related to the geometrical parameters of hard scatterers. First, the first two critical applied stretches increase with the increase of the cylinder's radius, which means a unit cell of PnC is more prone to instability with the addition of the radius of the cylinder. Second, with the parameter $\alpha_i$ tending to 1, the first two critical applied stretches decrease, which means a unit cell of PnC is more stable. On the contrary, the bigger the ratio of the semi-major axis and semi-minor axis is, the unit cell of PnC is more prone to instability. Third, the critical applied stretches are closely related to the arrangement of hard scatterers. It can be seen from Fig. 17 that the critical applied stretches of the unit cell shown in Fig. 12(*a*) is greater than those of the unit cell shown in Fig. 12(*b*), which means the unit cell shown in Fig. 12(*b*) is more stable in comparison with the unit cell shown in Fig. 12(*a*). In short, the unit cells presented in this paper can achieve the manipulation of elastic wave propagation while they can be used to design composites of different mechanical properties.

## Appendix C

Figure 18 shows the Bloch mode shapes at the frequency points of choice shown in Figs. 12(*a*), 12(*b*), 12(*c*), and 12(*d*) correspond to those in Fig. 12. Points i, ii, iii, and iv correspond to modes 12, 13, 20, and 21, respectively. It can be seen that their mode shapes have significant differences in the same modes. The results in columns (a) and (b) have been verified in Comsol Multiphysics 5.2a. These differences lead to the differences in the band structures and band gaps of PnCs.

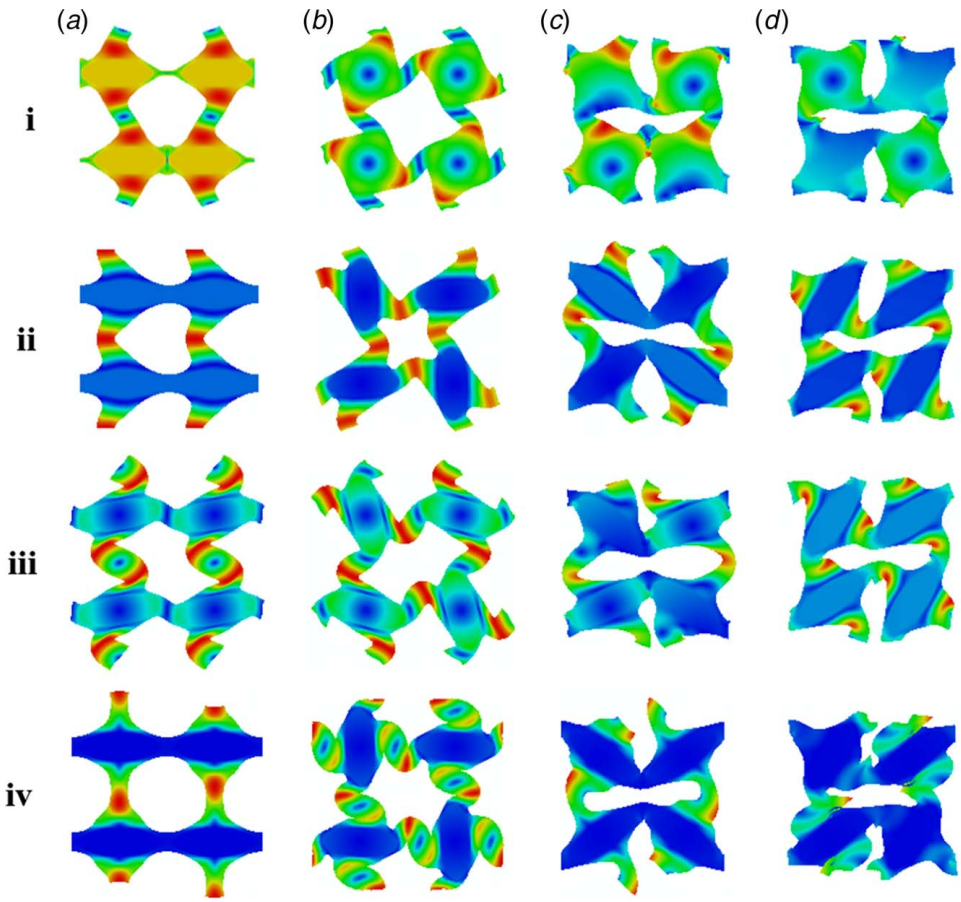


**Fig. 18 The Bloch mode shapes at the frequency points of choice shown in Figs. 12(a), 12(b), 12(c), and 12(d) corresponding to those in Fig. 12. Points i, ii, iii, and iv correspond to modes 12, 13, 20, and 21, respectively.**

## References


[1] Hussein, M. I., Leamy, M. J., and Ruzzene, M., 2014, "Dynamics of Phononic Materials and Structures: Historical Origins, Recent Progress, and Future Outlook," ASME Appl. Mech. Rev., **66**(4), p. 040802.

[2] Ge, H., Yang, M., Ma, C., Lu, M.-H., Chen, Y.-F., Fang, N., and Sheng, P., 2018, "Breaking the Barriers: Advances in Acoustic Functional Materials," Natl. Sci. Rev., **5**(2), pp. 159–182.

[3] Luo, C., Johnson, S. G., Joannopoulos, J. D., and Pendry, J. B., 2002, "All-Angle Negative Refraction Without Negative Effective Index," Phys. Rev. B, **65**(20), p. 201104.

[4] Qiu, C., Zhang, X., and Liu, Z., 2005, "Far-Field Imaging of Acoustic Waves by a Two-Dimensional Sonic Crystal," Phys. Rev. B, **71**(5), p. 054302.

[5] Chen, Z.-G., Zhao, J., Mei, J., and Wu, Y., 2017, "Acoustic Frequency Filter Based on Anisotropic Topological Phononic Crystals," Sci. Rep., **7**(1), p. 15005.

[6] Page, J. H., 2016, "Focusing of Ultrasonic Waves by Negative Refraction in Phononic Crystals," AIP Adv., **6**(12), p. 121606.

[7] Wang, Y.-F., Wang, T.-T., Liang, J.-W., Wang, Y.-S., and Laude, V., 2018, "Channeled Spectrum in the Transmission of Phononic Crystal Waveguides," J. Sound Vib., **437**, pp. 410–421.

[8] Dong, H.-W., Zhao, S.-D., Wang, Y.-S., and Zhang, C., 2018, "Broadband Single-Phase Hyperbolic Elastic Metamaterials for Super-Resolution Imaging," Sci. Rep., **8**(1), p. 2247.

[9] Zhao, S.-D., Chen, A.-L., Wang, Y.-S., and Zhang, C., 2018, "Continuously Tunable Acoustic Metasurface for Transmitted Wavefront Modulation," Phys. Rev. Appl., **10**(5), p. 054066.

[10] Casadei, F., Delpero, T., Bergamini, A., Ermanni, P., and Ruzzene, M., 2012, "Piezoelectric Resonator Arrays for Tunable Acoustic Waveguides and Metamaterials," J. Appl. Phys., **112**(6), p. 064902.

[11] Xiao, Y., Wen, J., and Wen, X., 2012, "Sound Transmission Loss of Metamaterial-Based Thin Plates With Multiple Subwavelength Arrays of Attached Resonators," J. Sound Vib., **331**(25), pp. 5408–5423.

[12] Casadei, F., Beck, B. S., Cunefare, K. A., and Ruzzene, M., 2012, "Vibration Control of Plates Through Hybrid Configurations of Periodic Piezoelectric Shunts," J. Intell. Mater. Syst. Struct., **23**(10), pp. 1169–1177.

[13] Yu, D., Wen, J., Zhao, H., Liu, Y., and Wen, X., 2008, "Vibration Reduction by Using the Idea of Phononic Crystals in a Pipe-Conveying Fluid," J. Sound Vib., **318**(1–2), pp. 193–205.

[14] Zhang, H., Wen, J., Xiao, Y., Wang, G., and Wen, X., 2015, "Sound Transmission Loss of Metamaterial Thin Plates With Periodic Subwavelength Arrays of Shunted Piezoelectric Patches," J. Sound Vib., **343**, pp. 104–120.

[15] Sun, Y., Li, Z., Huang, A., and Li, Q., 2015, "Semi-Active Control of Piezoelectric Coatings Underwater Sound Absorption by Combining Design of the Shunt Impedances," J. Sound Vib., **355**, pp. 19–38.

[16] Wang, G., Wang, J., Chen, S., and Wen, J., 2011, "Vibration Attenuations Induced by Periodic Arrays of Piezoelectric Patches Connected by Enhanced Resonant Shunting Circuits," Smart Mater. Struct., **20**(12), p. 125019.

[17] Huang, Z. G., and Wu, T. T., 2005, "Temperature Effect on the Bandgaps of Surface and Bulk Acoustic Waves in Two-Dimensional Phononic Crystals," IEEE Trans. Ultrason. Ferroelectr. Freq. Control, **52**(3), pp. 365–370.

[18] Xia, B., Chen, N., Xie, L., Qin, Y., and Yu, D., 2016, "Temperature-Controlled Tunable Acoustic Metamaterial With Active Band Gap and Negative Bulk Modulus," Appl. Acoust., **112**, pp. 1–9.

[19] Yao, Y., Wu, F., Zhang, X., and Hou, Z., 2011, "Thermal Tuning of Lamb Wave Band Structure in a Two-Dimensional Phononic Crystal Plate," J. Appl. Phys., **110**(12), p. 123503.

[20] Jim, K. L., Leung, C. W., Lau, S. T., Choy, S. H., and Chan, H. L. W., 2009, "Thermal Tuning of Phononic Bandstructure in Ferroelectric Ceramic/Epoxy Phononic Crystal," Appl. Phys. Lett., **94**(19), p. 193501.

[21] Vasseur, J. O., Matar, O. B., Robillard, J. F., Hladky-Hennion, A.-C., and Deymier, P. A., 2011, "Band Structures Tunability of Bulk 2D Phononic Crystals Made of Magneto-Elastic Materials," AIP Adv., **1**(4), p. 041904.

[22] Bou Matar, O., Robillard, J. F., Vasseur, J. O., Hladky-Hennion, A.-C., Deymier, P. A., Pernod, P., and Preobrazhensky, V., 2012, "Band Gap Tunability of Magneto-Elastic Phononic Crystal," J. Appl. Phys., **111**(5), p. 054901.

[23] Zhang, S., Shi, Y., and Gao, Y., 2017, "Tunability of Band Structures in a Two-Dimensional Magnetostrictive Phononic Crystal Plate With Stress and Magnetic Loadings," Phys. Lett. Sect. A Gen. At. Solid State Phys., **381**(12), pp. 1055–1066.

[24] Zhang, S., and Gao, Y., 2019, "Tunability of Hysteresis-Dependent Band Gaps in a Two-Dimensional Magneto-Elastic Phononic Crystal Using Magnetic and Stress Loadings," Appl. Phys. Express, **12**(2), p. 027001.

[25] Ding, R., Su, X., Zhang, J., and Gao, Y., 2014, "Tunability of Longitudinal Wave Band Gaps in One Dimensional Phononic Crystal With Magnetostrictive Material," J. Appl. Phys., **115**(7), p. 074104.

[26] Zhang, S., and Gao, Y., 2018, "Gap Evolution of Lamb Wave Propagation in Magneto-Elastic Phononic Plates With Pillars and Holes by Modulating Magnetic Field and Stress Loadings," J. Appl. Phys., **124**(24), p. 244102.

[27] Wu, B., Zhou, W., Bao, R., and Chen, W., 2018, "Tuning Elastic Waves in Soft Phononic Crystal Cylinders Via Large Deformation and Electromechanical Coupling," ASME J. Appl. Mech., **85**(3), p. 031004.

[28] Xu, J., and Tang, J., 2017, "Tunable Prism Based on Piezoelectric Metamaterial for Acoustic Beam Steering," Appl. Phys. Lett., **110**(18), p. 181902.

[29] Gao, N., Li, J., Bao, R., and Chen, W., 2019, "Harnessing Uniaxial Tension to Tune Poisson's Ratio and Wave Propagation in Soft Porous Phononic Crystals: An Experimental Study," Soft Matter, **15**(14), pp. 2921–2927.

[30] Nguyen, B. H., Zhuang, X., Park, H. S., and Rabczuk, T., 2019, "Tunable Topological Bandgaps and Frequencies in a Pre-Stressed Soft Phononic Crystal," J. Appl. Phys., **125**(9), p. 095106.

[31] Ning, S., Yang, F., Luo, C., Liu, Z., and Zhuang, Z., 2020, "Low-Frequency Tunable Locally Resonant Band Gaps in Acoustic Metamaterials Through Large Deformation," Extrem. Mech. Lett., **35**, p. 100623.

[32] Shim, J., Wang, P., and Bertoldi, K., 2015, "Harnessing Instability-Induced Pattern Transformation to Design Tunable Phononic Crystals," Int. J. Solids Struct., **58**, pp. 52–61.

[33] Li, J., Slesarenko, V., and Rudykh, S., 2018, "Auxetic Multiphase Soft Composite Material Design Through Instabilities With Application for Acoustic Metamaterials," Soft Matter, **14**(30), pp. 6171–6180.

[34] Zhou, W., Wu, B., Muhammad, Du, Q., Huang, G., Lü, C., and Chen, W., 2018, "Actively Tunable Transverse Waves in Soft Membrane-Type Acoustic Metamaterials," J. Appl. Phys., **123**(16), p. 165304.

[35] Wang, P., Shim, J., and Bertoldi, K., 2013, "Effects of Geometric and Material Nonlinearities on Tunable Band Gaps and Low-Frequency Directionality of Phononic Crystals," Phys. Rev. B, **88**(1), p. 014304.

[36] Shan, S., Kang, S. H., Wang, P., Qu, C., Shian, S., Chen, E. R., and Bertoldi, K., 2014, "Harnessing Multiple Folding Mechanisms in Soft Periodic Structures for Tunable Control of Elastic Waves," Adv. Funct. Mater., **24**(31), pp. 4935–4942.

[37] Li, J., Wang, Y., Chen, W., Wang, Y.-S., and Bao, R., 2019, "Harnessing Inclusions to Tune Post-Buckling Deformation and Bandgaps of Soft Porous Periodic Structures," J. Sound Vib., **459**, p. 114848.

[38] Bertoldi, K., and Boyce, M. C., 2008, "Wave Propagation and Instabilities in Monolithic and Periodically Structured Elastomeric Materials Undergoing Large Deformations," Phys. Rev. B, **78**(18), p. 184107.

[39] Zhong, L., Wu, F., Zhang, X., Zhong, H., and Zhong, S., 2005, "Effects of Orientation and Symmetry of Rods on the Complete Acoustic Band Gap in Two-Dimensional Periodic Solid/Gas Systems," Phys. Lett. Sect. A Gen. At. Solid State Phys., **339**(1–2), pp. 164–170.

[40] Dong, H., Wu, F., Zhong, H., Zhang, X., and Yao, Y., 2010, "Effects of Asymmetrical Rotated Rectangular Basis on the Acoustic Band Gap in Two-Dimensional Acoustic Crystals: The Bands Are Twisted," J. Phys. D. Appl. Phys., **43**(10), p. 105404.

[41] Wu, L. Y., and Chen, L. W., 2007, "The Dispersion Characteristics of Sonic Crystals Consisting of Elliptic Cylinders," J. Phys. D. Appl. Phys., **40**(23), pp. 7579–7583.

[42] Wu, F., Liu, Z., and Liu, Y., 2002, "Acoustic Band Gaps Created by Rotating Square Rods in a Two-Dimensional Lattice," Phys. Rev. E, **66**(4), p. 046628.

[43] Goffaux, C., and Vigneron, J. P., 2001, "Theoretical Study of a Tunable Phononic Band Gap System," Phys. Rev. B, **64**(7), p. 075118.

[44] Lee, J.-H., Wang, L., Boyce, M. C., and Thomas, E. L., 2012, "Periodic Bicontinuous Composites for High Specific Energy Absorption," Nano Lett., **12**(8), pp. 4392–4396.

[45] Maldovan, M., 2013, "Sound and Heat Revolutions in Phononics," Nature, **503**(7475), pp. 209–217.

[46] Maldovan, M., 2013, "Narrow Low-Frequency Spectrum and Heat Management by Thermocrystals," Phys. Rev. Lett., **110**(2), p. 025902.

[47] Liu, Y., Su, J.-Y., Xu, Y.-L., and Zhang, X.-C., 2009, "The Influence of Pore Shapes on the Band Structures in Phononic Crystals With Periodic Distributed Void Pores," Ultrasonics, **49**(2), pp. 276–280.

[48] Ning, S., Luo, C., Yang, F., Liu, Z., and Zhuang, Z., 2020, "Mechanically Tunable Solid/Solid Phononic Crystals Through the Rearrangement of Hard Scatterers Controlled by the Deformation of Periodic Elastomeric Matrixes," ASME J. Appl. Mech., **87**(10), p. 101002.

[49] Michel, J. C., Lopez-Pamies, O., Ponte Castañeda, P., and Triantafyllidis, N., 2007, "Microscopic and Macroscopic Instabilities in Finitely Strained Porous Elastomers," J. Mech. Phys. Solids, **55**(5), pp. 900–938.

[50] Bertoldi, K., Boyce, M. C., Deschanel, S., Prange, S. M., and Mullin, T., 2008, "Mechanics of Deformation-Triggered Pattern Transformations and Superelastic Behavior in Periodic Elastomeric Structures," J. Mech. Phys. Solids, **56**(8), pp. 2642–2668.

[51] Ruzzene, M., Scarpa, F., and Soranna, F., 2003, "Wave Beaming Effects in Two-Dimensional Cellular Structures," Smart Mater. Struct., **12**(3), pp. 363–372.

[52] Casadei, F., and Rimoli, J. J., 2013, "Anisotropy-Induced Broadband Stress Wave Steering in Periodic Lattices," Int. J. Solids Struct., **50**(9), pp. 1402–1414.

[53] Trainiti, G., Rimoli, J. J., and Ruzzene, M., 2016, "Wave Propagation in Undulated Structural Lattices," Int. J. Solids Struct., **97–98**, pp. 431–444.

[54] Gent, A. N., 1996, "A New Constitutive Relation for Rubber," Rubber Chem. Technol., **69**(1), pp. 59–61.

[55] Krushynska, A. O., Kouznetsova, V. G., and Geers, M. G. D., 2016, "Visco-Elastic Effects on Wave Dispersion in Three-Phase Acoustic Metamaterials," J. Mech. Phys. Solids, **96**, pp. 29–47.

[56] Hussein, M. I., and Frazier, M. J., 2013, "Metadamping: An Emergent Phenomenon in Dissipative Metamaterials," J. Sound Vib., **332**(20), pp. 4767–4774.

[57] DePauw, D., Al Ba'ba'a, H., and Nouh, M., 2018, "Metadamping and Energy Dissipation Enhancement via Hybrid Phononic Resonators," Extrem. Mech. Lett., **18**, pp. 36–44.